Morphological PDEs with Rotationally Invariant Space-Fractional Derivatives

Martin Welk[1 [0000−0002−6268−7050]], Andreas Kleefeld[2,3 [0000−0001−8324−821X]], Michael Breuß[4 [0000−0002−5322−2411]], and Bernhard Burgeth[5 [0000−0001−6602−6201]]

[1] UMIT TIROL – Private University of Health Sciences and Health Technology, Eduard-Wallnöfer-Zentrum 1, 6060 Hall/Tyrol, Austria
martin.welk@umit-tirol.at
[2] Forschungszentrum Jülich GmbH, Jülich Supercomputing Centre, Wilhelm-Johnen-Straße, 52425 Jülich, Germany
a.kleefeld@fz-juelich.de
[3] University of Applied Sciences Aachen, Faculty of Medical Engineering and Technomathematics, Heinrich-Mußmann-Straße 1, 52428 Jülich, Germany
[4] Institute for Mathematics, Brandenburg University of Technology Cottbus-Senftenberg, 03046 Cottbus, Germany
breuss@b-tu.de
[5] Department of Mathematics and Computer Science, Saarland University, 66041 Saarbrücken, Germany
burgeth@math.uni-sb.de

Abstract. The spatial derivatives in Hamilton-Jacobi partial differential equations for the definition of morphological operations such as dilation and erosion for grey-value images are replaced by fractional derivatives of arbitrary positive order. Focus is laid on geometric invariance with respect to reflections and rotations so that directional bias towards the coordinate directions is avoided. Discretisation of directional fractional derivatives via truncated general power series ultimately leads to an optimisation problem for the advection direction. We numerically compare the proposed fractional morphological operations with conventional counterparts and a simpler fractional-order alternative on grey-value images to show interesting phenomena and gain insights into the effects of the non-local nature of the fractional derivatives which merit further investigation.

Keywords: PDE-based morphology · fractional derivative · shock filter

1 Introduction

Morphological dilation and erosion for continuous-scale grey-value images $u : \mathbb{R}^2 \to \mathbb{R}$ can be described by the well-known Hamilton-Jacobi partial differential equations (PDEs)

$$u_t = |\boldsymbol{\nabla} u| \quad \text{(dilation)}, \qquad u_t = -|\boldsymbol{\nabla} u| \quad \text{(erosion)} \tag{1}$$

where $|\boldsymbol{\nabla} u|$ is the Euclidean norm of the spatial gradient of u, see e.g. [3, 4, 9]. Using a given image f as initial condition $u(t = 0) = f$, these PDEs yield for $t > 0$ dilated/eroded variants of f with disc-shaped structuring elements of radius t. It is worth

In M. H. F. Wilkinson, J. Kosinka (eds.): Discrete Geometry and Mathematical Morphology (DGMM 2025), Lecture Notes in Computer Science, vol. 16296, pp. 401–414, Springer, Cham, 2025.
The final publication is available at link.springer.com .

noticing here that $\pm|\boldsymbol{\nabla} u|$ are the maximum and minimum, respectively, among the directional derivatives of u in all possible spatial directions, see also eqs. (26), (27) of [4]. Therefore (1) are advection PDEs in which the advection direction is determined at each location is that of the greatest or smallest directional derivative.

Several generalisations and modifications of these PDEs have been studied in literature. In this work, we are interested in studying variants in which the spatial gradient is replaced by fractional derivatives.

Fractional-order differentiation goes back to the very origins of calculus itself as already Leibniz has discussed how to do, say, a half-order derivative instead of integer derivative orders, see [15] for a historical overview and [15, 18] for detailed definitions and derivations. One approach to defining a fractional derivative of a (absolutely and square integrable and sufficiently regular) function $f : \mathbb{R} \to \mathbb{R}$ is based on the Fourier transform $\mathcal{F}[f] : \mathbb{R} \to \mathbb{C}$ of f and the identity $\mathcal{F}[\partial_x^k f](\xi) = (\mathrm{i}\xi)^k \mathcal{F}[f](\xi)$ for derivatives of integer order. With the disambiguation $\mathrm{i}^\alpha := \exp(\mathrm{i}\alpha\pi/2)$ (principal value) one can define $\partial_x^\alpha f := \mathcal{F}^{-1}[(\mathrm{i}\xi)^\alpha \mathcal{F}[f]]$ for real $\alpha > 0$. Alternative definitions are the Riemann-Liouville derivative given by an integro-differential operator,

$$\partial_x^\alpha f(x) = \frac{1}{\Gamma(k-\alpha)} \partial^k \int_{-\infty}^{x} (x-y)^{k-\alpha-1} f(y)\,\mathrm{d}y\,, \quad k := \lfloor \alpha \rfloor + 1\,, \tag{2}$$

with Γ denoting the standard gamma function, and $\lfloor \alpha \rfloor$ denoting the greatest integer not greater than α, or the similarly defined Caputo derivative. All three definitions coincide in those cases where all of them are defined. For numerical evaluation on sampled data, discretisations are available, with the Grünwald-Letnikov derivatives (see Section 2) as a prominent example.

Unlike ordinary derivatives, fractional derivatives of non-integer order are non-local in that their values at some location x do not depend just on f in a neighbourhood of x but on its values on the entire real half-axis $(-\infty, x]$. In applications, this is a reasonable choice for derivatives w.r.t. the time coordinate which then obey temporal causality. Indeed, time-fractional differential equations have proven useful in applications such as diffusion in porous media [8] or damped oscillators [2, 20], where the non-locality acts to model memory effects or delayed responses. When considering fractional derivatives in space, e.g. for space-fractional diffusion [5], preference for one real half-axis is often unphysical, leading to the consideration of symmetrised fractional derivative concepts [19]. Still, space-fractional PDEs in two or three spatial dimensions are mostly based on combining 1D fractional derivatives w.r.t. coordinate directions [5, 17, 23, 27].

Fractional differential equations have also been considered in the context of image processing [1, 26]. On one hand, time-fractional differential equations can profit from the same benefits of modeling memory or delay by causal time derivatives, see e.g. [13] for time-fractional morphological PDEs. On the other hand, space-fractional derivatives allow to introduce an interesting kind of controlled non-local behaviour into image processing. Space-fractional derivatives have been used e.g. for edge detection [22], denoising and image enhancement [11, 12, 29], regularisation [6, 7, 24], segmentation [21] or image super-resolution [10].

Many of these approaches use symmetric space-fractional derivatives; however, the majority of works we are aware of adhere to the use of 1D fractional derivatives in

coordinate directions. Given the importance of spatial symmetries in image processing, we question this approach: Whereas ordinary derivatives in two or three dimensions can be broken down to derivative operators w.r.t. the coordinates, proceeding similarly for non-local fractional derivatives can be expected to introduce strong directional bias towards the coordinate directions.

In an attempt to mitigate these problems, some authors introduce additional directional derivatives in 45 degree steps [11, 21, 26]. In [25], the approach is refined by using 22.5 degree steps by applying a 1D fractional derivative discretisation to a series of intensity values interpolated from grid values.

A rare instance of consequently envisioning rotational invariance is found in [7] where fractional powers of the negative Laplacian are computed via the Fourier domain and used as rotationally symmetric operators for fractional diffusion and regularisation.

Our contribution. We establish a framework for discrete approximations of space-fractional derivatives for 2D morphology with emphasis on geometric invariance w.r.t. reflections and rotations. In particular, we propose a novel concept of directional fractional derivatives in arbitrary directions from which we construct fractional counterparts of the r.h.s. of Hamilton-Jacobi equations for dilation and erosion. We discuss qualitative properties of the resulting fractional dilation and erosion operations. In particular, the use of space-fractional derivatives extends the classical concept of *morphology* as *shape-based* processing in the sense that due to their non-locality, the resulting filters look to a certain extent *below the surface* of the evolving shapes. We present experiments to confirm and extend these findings, including also composed operators such as opening, closing and morphological shock filters, juxtaposing them with standard morphological operations. As we are interested in the potential of space-fractional morphology, comparisons with time-fractional approaches are not in our scope here.

Structure of the paper. In Section 2, we recall the discretisation of fractional derivatives using the Grünwald-Letnikov formula. We discuss how symmetry can be incorporated when using fractional derivatives for morphological PDEs which is then applied to 1D signals first. Then, the extension to the 2D case is derived based on a truncated general power series and an optimisation over advection directions. In Section 3, numerical results for dilation, erosion, opening, closing, and shock filters for a variety of grey-value images with different fractional derivative orders are presented to illustrate their effects. A short conclusion and outlook to future work is given in Section 4.

2 Fractional Derivatives

We start by recalling essential facts on 1D fractional derivatives with emphasis on the specifics of morphological image processing. Based on this, we then propose a 2D extension fitting this purpose.

2.1 The 1D Case

Standard (backward) Grünwald-Letnikov derivatives. The basic form of a Grünwald-Letnikov discretised derivative of order $\alpha > 0$ for a sampled 1D signal with

spatial step size h and values $u_i = u(x_0 + ih)$ is

$$[\partial^\alpha_{x-} u]_i = h^{-\alpha} \sum_{k=0}^{\infty} (-1)^k \binom{\alpha}{k} u_{i-k} \tag{3}$$

with the binomial coefficients $\binom{\alpha}{k} := \frac{\alpha(\alpha-1)\cdots(\alpha-k+1)}{k!}$. For a detailed derivation see e.g. [15]. The coefficients of (3) can be read off the power series

$$(1-x)^\alpha = \sum_{k=0}^{\infty} (-1)^k \binom{\alpha}{k} x^k \,. \tag{4}$$

In the case of integer order $\alpha > 0$ (where the series is finite) this is a direct consequence of the fact that multiplication of polynomials or power series is equivalent to a convolution of their coefficient sequences and thus to the iterated convolution of the backward finite difference discretisation $[\partial_{x-} u]_i = (u_i - u_{i-1})/h$. For non-integer orders the power series thus offers a natural way to interpolate between the integer order convolutions.

Under suitable regularity assumptions, the Grünwald-Letnikov derivative converges to the continuous-scale (e.g. Riemann-Liouville) derivative as the grid is refined, $h \to 0$. Moreover, for positive integer order α one has a backward-difference approximation for the ordinary derivative $\partial^\alpha_x u(x)$.

For non-integer α, the derivative is non-local, and in the given form, it looks backward on the real axis. In applications, this is a reasonable choice for time-fractional differential equations which then are guaranteed to obey temporal causality. When aiming at spatial fractional derivatives for image processing applications, however, it is paramount to ensure compatibility with spatial symmetries and therefore to consider also forward-looking and possibly spatially symmetric derivatives.

Forward and symmetric fractional derivatives. In principle, forward-looking derivatives can be defined by reverting the real axis, i.e. applying the derivatives as before to the function $\tilde{u}(x) := u(-x)$. However, noticing that for ordinary derivatives of integer order α one has $\partial^\alpha_x \tilde{u}(-x) = (-1)^\alpha \partial^\alpha_x u(x)$, the question arises how to treat the sign factor $(-1)^\alpha$ for non-integer α. Defining a forward-looking derivative as $\partial^\alpha_{x+} u(x) = (-1)^\alpha \partial^\alpha_{x-} \tilde{u}(-x)$ (where $(-1)^\alpha$ requires disambiguation, e.g. as $\exp(\mathrm{i}\pi\alpha)$) makes it complex-valued even for real-valued functions which is cumbersome for applications. Alternatively, one can drop the complex sign factor. One can then either impose even symmetry for all orders α by $\partial^\alpha_{x+} u(x) = \partial^\alpha_{x-} \tilde{u}(-x)$, or impose odd symmetry for all orders α by $\partial^\alpha_{x+} u(x) = -\partial^\alpha_{x-} \tilde{u}(-x)$. The first choice, even symmetry, ensures correct embedding of derivatives of even integer order, $\partial^\alpha_{x+} u(x) = \partial^\alpha_x u(x)$, but leads to a sign-reversal for odd integer orders, $\partial^\alpha_{x+} u(x) = -\partial^\alpha_x u(x)$. The odd symmetry choice correctly embeds odd integer orders but involves sign reversal for even integer orders. We remark that the even-symmetric variant can be associated with the pseudo-differential operators $-(-\partial_{xx})^{\alpha/2}$, compare [7].

Symmetric derivatives can either be obtained by combining backward and forward derivatives or by directly generalising central finite difference approximations. The difficulties regarding the choice between even and odd symmetry remain and lead to different models proposed in literature [14, 16, 19, 24, 28].

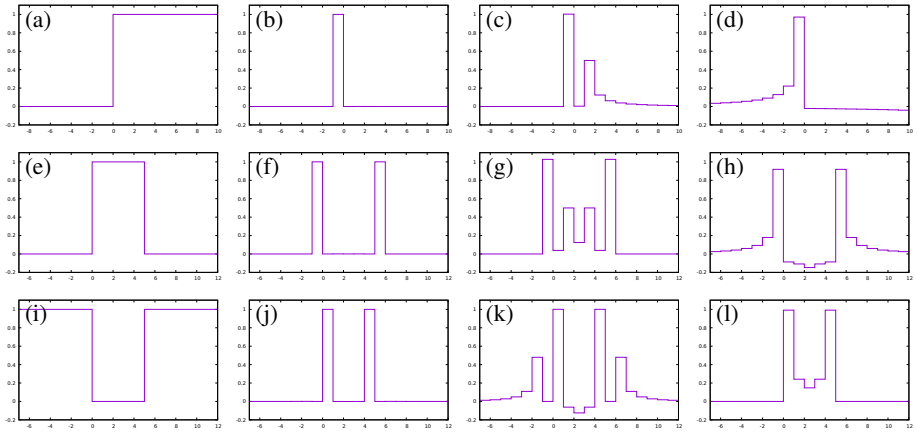

Fig. 1. Dilation PDE r.h.s. of simple discrete 1D signals with spatial step size 1. **Top to bottom:** (a–d) Heaviside signal; (e–h) high impulse of width 5; (i–l) low impulse of width 5. **Left to right:** (a, e, i) signal f; (b, f, j) upwind approximation of $|f_x|$; (c, g, k) fractional derivative $|\partial_x^{1.5} f(x)|_+$; (d, h, l) fractional derivative $|\partial_x^{0.75} f(x)|_+$. Horizontal axis shows space coordinate, vertical axis shows intensity.

Fractional derivatives for morphological PDEs. Fortunately, for our goal of generalising PDEs of mathematical morphology we can avoid the aforementioned problems. The quantity we actually want to generalise is $|\partial_x u| = \max\{\partial_x u, -\partial_x u\}$, and it is commonly discretised in upwind schemes by one-sided finite differences, switching between forward and backward differences based on sign. Defining the forward derivative as $\partial^\alpha_{x+} u(x) = -\partial^\alpha_{x-} \tilde{u}(-x)$, we have $|\partial^\alpha_x u(x)|_+ := \max\{-\partial^\alpha_{x-} u(x), \partial^\alpha_{x+} u(x)\}$ as a generalisation of $|\partial_x u|$ that always looks into the half-axis from which higher values are advected, thus suitable for morphological dilation, or $|\partial^\alpha_x u(x)|_- := \max\{\partial^\alpha_{x-} u(x), -\partial^\alpha_{x+} u(x)\}$ which always looks into the half-axis from which lower values are advected, as appropriate for morphological erosion. We can therefore write down the 1D space-fractional morphological dilation PDE $u_t = |\partial^\alpha_x u(x)|_+$ and the 1D space-fractional morphological erosion PDE $u_t = -|\partial^\alpha_x u(x)|_-$.

2.2 Behaviour of Fractional Dilation in 1D

We analyse the responses of the r.h.s. of the 1D space-fractional dilation equation $u_t = \max\{\partial^\alpha_{x+} u, -\partial^\alpha_{x-} u\}$ to discrete Heaviside functions ($u_i = 0$ for $i < 0$, $u_i = 1$ for $i \geq 0$), high flip impulses ($u_i = 1$ for $0 \leq i \leq w$, $u_i = 0$ otherwise) and low flip impulses ($u_i = 0$ for $0 \leq i \leq w$, $u_i = 1$ otherwise). Fractional derivative stencils were truncated at distance 100, which is far beyond the length of all involved structures and ensures negligible truncation errors.

We first consider $\alpha = 1$. In this case, the fractional derivative becomes a standard derivative which is approximated by an upwind approximation. This leads to a peak of size 1 shifted one unit to the left for the Heaviside function (see Fig. 1(b)). For the high flip impulse of size 5, we obtain two peaks of size 1. Here, the left peak is shifted one

unit to the left whereas the right peak is shifted one unit to the right (Fig. 1(f)). For the low flip impulse of size 5, we also obtain two peaks of size 1. However, the left peak is shifted one unit to the right whereas the left peak is shifted one unit to the left (Fig. 1(j)).

Next, we consider the case $\alpha \in (1,2)$. As an example, we choose $\alpha = 1.5$. Here, the situation for the Heaviside function leads to the same result as for $\alpha = 1$ except that there is an additional positive decaying tail one unit right at the discontinuity of the Heaviside function (see Fig. 1(c)). This leads to an enhancement of an edge and a violation of the maximum principle. For the high impulse, we obtain the same peaks as for $\alpha = 1$ with the exception that the peaks are slightly larger than 1. Between the two peaks smaller peaks arise (Fig. 1(g)), again entailing a violation of the maximum principle. For the low impulse, we obtain the same two peaks as for $\alpha = 1$ and the same positive decaying tails to the left of the left peak and to the right of the right peak, respectively (Fig. 1(k)). Inbetween the two peaks, the results get negative. Hence, the minimum principle is violated. In total, the expected effects for dilation are enhancement of edges and the enhancement of thin bright line structures. Further, dilation is slowed at thin dark line structures which preserves them longer. Overall, we observe some reduction of numerical dissipation when compared to standard dilation ($\alpha = 1$).

Finally, we consider the case $\alpha \in (0,1)$. We choose $\alpha = 0.75$ as an example. For the Heaviside function, we obtain a peak left to the discontinuity with a decaying tail on the left of this peak. Interestingly, we also obtain a tail to the right with small negative decaying values (see Fig. 1(d)). Hence, the minimum principle is violated. For the high impulse, we obtain two peaks left and right of the discontinuity, but the height is smaller than one. We observe two decaying tails to the left of the left peak and to the right of the right peak. Inbetween the two peaks, we obtain negative values (Fig. 1(h)). For the low flip impulse, we obtain the same two peaks as for $\alpha = 1$ with the exception that inbetween the peaks mass larger than zero appears (Fig. 1(l)). In total, the expected effects for dilation are contrast reduction as well as increased blurring effects.

2.3 Extension to 2D

As we set out to generalise the PDEs of morphological dilation and erosion in which the gradient norm acts to maximise or minimise, respectively, over directional derivatives, we are led to devise as the first step a fractional counterpart of a directional derivative in direction of a unit vector $\boldsymbol{e}_\varphi := (\cos\varphi, \sin\varphi)^{\mathrm{T}}$, $\varphi \in [0, 2\,\pi]$.

For $\varphi \in [0, \pi/2]$ a spatial discretisation of the first derivative in the direction of $\boldsymbol{e}_\varphi$ with forward finite differences in x and y direction reads as

$$[\partial_{\boldsymbol{e}_\varphi} u]_{i,j} = \cos\varphi \, \frac{u_{i+1,j} - u_{i,j}}{h} + \sin\varphi \, \frac{u_{i,j+1} - u_{i,j}}{h} \; . \tag{5}$$

By a similar reasoning as in the one-dimensional case, a discretised derivative of order α in the same direction is obtained as

$$[\partial^\alpha_{\boldsymbol{e}_\varphi} u]_{i,j} = h^{-\alpha} \sum_{k,l=0}^{\infty} d^\alpha_{\varphi;k,l} u_{i+k,j+l} \tag{6}$$

where the coefficients $d^{\alpha}_{\varphi;k,l}$ are those from the power series in two variables

$$-((\cos\varphi+\sin\varphi)-\cos\varphi\cdot x-\sin\varphi\cdot y)^{\alpha}=\sum_{k,l=0}^{\infty}d^{\alpha}_{\varphi;k,l}x^k y^l\ , \tag{7}$$

$$d^{\alpha}_{\varphi;k,l}=(-1)^{k+l+1}\binom{\alpha}{k,l}(\cos\varphi)^k(\sin\varphi)^l(\cos\varphi+\sin\varphi)^{\alpha-k-l}\ , \tag{8}$$

$$k,l=0,1,\ldots,\quad \varphi\in[0,\pi/2] \tag{9}$$

with the trinomial coefficients $\binom{\alpha}{k,l}:=\binom{\alpha}{k}\binom{\alpha-k}{l}$.

This is of course an infinite-size stencil that needs to be cut off at some finite length. Due to the rather slow decay of the coefficients with k and l reasonable stencil sizes involve a significant cut-off error which needs to be compensated to ensure that the numerical approximation of the fractional derivative does not incur an unnatural dependency on absolute intensity levels. We do this by adjusting the coefficient $d^{\alpha}_{\varphi;0,0}$, i.e. we use $d^{\alpha}_{\varphi;k,l}$ for $k=0,\ldots,K$, $l=0,\ldots,L$, $(k,l)\neq(0,0)$ and replace $d^{\alpha}_{\varphi;0,0}$ with $\tilde{d}^{\alpha}_{\varphi;0,0}=-\sum_{k,l=0;k+l\geq 1}^{K,L}d^{\alpha}_{\varphi;k,l}$.

For directions $\varphi\in[\pi/2,2\pi]$ the same type of stencil is applied in the other quadrants, i.e. replacing $u_{i+l,j+l}$ in (6) with $u_{i+k,j-l}$, $u_{i-k,j+l}$ or $u_{i-k,j-l}$ as appropriate. On quadrant boundaries, the discretisations from both adjacent quadrants collapse to the same 1D Grünwald-Letnikov discretisation.

In the terms of our discussion of even/odd symmetry of fractional derivatives in the 1D case, we notice that $[\partial_{\boldsymbol{e}_\varphi}u]_{i,j}$ behaves as an odd-symmetric generalisation since one has $[\partial_{-\boldsymbol{e}_\varphi}u]_{i,j}=-[\partial_{\boldsymbol{e}_\varphi}\tilde{u}]_{-i,-j}$ where $\tilde{u}_{i,j}=u_{-i,-j}$ is the point-reflected image.

Altogether this can be used for an approximation of the fractional dilation PDE

$$u_t=|\boldsymbol{\nabla}^{\alpha}u|_+:=\max_{\varphi\in[0,2\pi)}\partial^{\alpha}_{\boldsymbol{e}_\varphi}u\ , \tag{10}$$

and similarly $u_t=-|\boldsymbol{\nabla}^{\alpha}u|_-:=\min_{\varphi\in[0,2\pi)}\partial^{\alpha}_{\boldsymbol{e}_\varphi}u$ for erosion. As in the 1D case, the maximum makes $|\boldsymbol{\nabla}^{\alpha}u|_+$ always look into the direction from which the highest values are advected, whereas $-|\boldsymbol{\nabla}^{\alpha}u|_-$ uses the minimum to detect the direction from which the lowest values are advected.

Unfortunately, the determination of the maximum in (10) requires some effort. Whereas for integer derivative orders, directional derivatives at a given point depend on the orientation angle just by low-order harmonics (such as a single sine wave for first order, and a double sine wave for second order), fractional directional derivatives can have multiple local maxima and minima over the orientation range $[0,2\pi]$. We use therefore a brute-force maximisation over sampled orientations for a full maximisation, which comes at a significant computational expense, and leave efficiency optimisations for future work. As a faster alternative, we consider an approach in which the direction of the standard (first-order) gradient vector is used to guide the direction of the fractional derivative. In effect, this replaces the fractional dilation PDE (10) with

$$u_t=|\partial^{\alpha}_{\boldsymbol{e}_\varphi}u|_+\ ,\quad \boldsymbol{e}_\varphi=(\cos\varphi,\sin\varphi)=\tfrac{\boldsymbol{\nabla}u}{|\boldsymbol{\nabla}u|}\ , \tag{11}$$

with $\boldsymbol{\nabla}u$ approximated by central differences, and similarly for erosion. We will compare these two variants of fractional morphological operations in our experiments. To

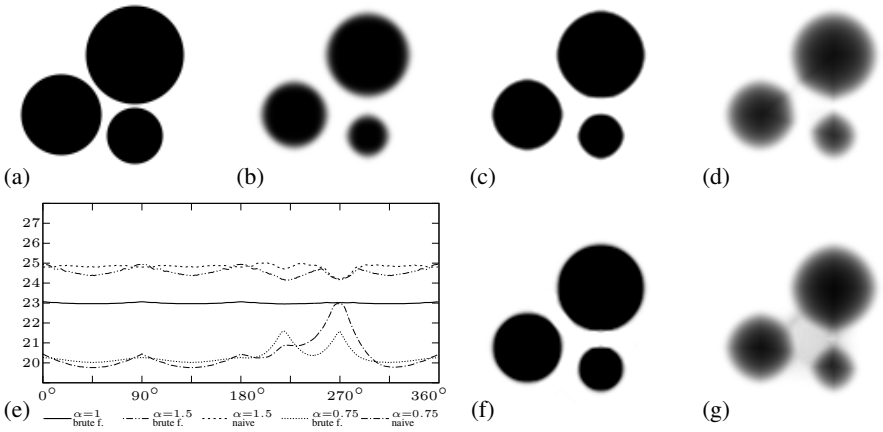

Fig. 2. Standard and fractional PDE-based dilation PDE of a synthetic grey-scale image. All dilations computed by an Euler forward scheme with time step size $\tau = 0.1$ and 50 iterations with brute-force maximisation (top row) or naive method (bottom row). (a) test image, 128×128 pixels; (b) standard dilation ($\alpha = 1$); (c, f) fractional dilation, $\alpha = 1.5$; (d, g) fractional dilation, $\alpha = 0.75$. (e) angular profiles of radii of dilated top-right discs.

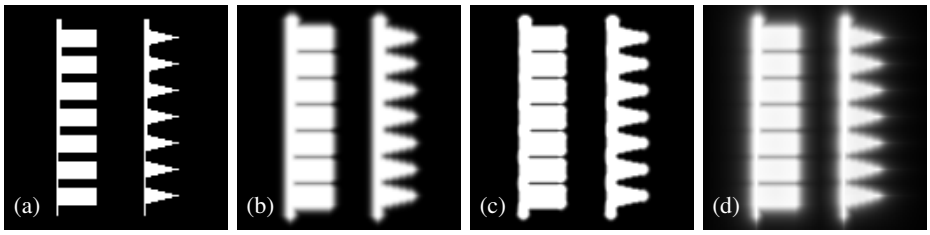

Fig. 3. Standard and fractional PDE-based dilation PDE of a synthetic grey-scale image. All dilations computed by an Euler forward scheme with time step size $\tau = 0.1$ and 30 iterations with brute-force maximisation. **Left to right:** (a) test image, 128×128 pixels; (b) standard dilation ($\alpha = 1$); (c) fractional dilation, $\alpha = 1.5$; (d) fractional dilation, $\alpha = 0.75$.

put the method in context with existing work, we also formulate a *naive* method following the popular approach of combining 1D fractional derivatives in grid directions:

$$u_t = |\cos\varphi| \cdot |\partial^{\alpha}_{(\operatorname{sgn}\cos\varphi,0)} u|_+ + |\sin\varphi| \cdot |\partial^{\alpha}_{(0,\operatorname{sgn}\sin\varphi)} u|_+ \tag{12}$$

with $(\cos\varphi, \sin\varphi)^{\mathrm{T}} = \boldsymbol{\nabla} u / |\boldsymbol{\nabla} u|$, where the axial fractional derivatives collapse to 1D fractional derivatives, and similarly for erosion.

3 Experiments

Synthetic test images. In our first series of experiments, see Figs. 2 and 3, we compare standard and fractional dilation on two test images designed to demonstrate theoreti-

cally predicted phenomena. The first of these images, Fig. 2(a), shows three black discs against white background that will be shrunk by all variants of PDE-based dilation. We show standard dilation (b), dilation with $\alpha = 1.5$ as an example of $1 < \alpha < 2$ (c), and dilation with $\alpha = 0.75$ as an example of $0 < \alpha < 1$ (d), all computed via brute-force maximisation. Here we truncate the stencils to 30 steps in both x and y direction. The cut-off value is chosen such that both the individual neglected coefficients and their total are small enough to expect no significant influence on the image. For a cut-off of 30 steps, none of the neglected coefficients is greater than 10^{-4}, and their total does not exceed 0.002. Also, experiments with different cut-off values confirm that while there are tiny visual differences in results where the cut-off size is reduced to 10 steps but with cut-offs of 20 and more steps results are visually indistinguishable.

For comparison, we show also results of the naive fractional dilation method with $\alpha = 1.5$ (f), and $\alpha = 0.75$ (g). In Fig. 2(e), we display angular profiles of the radii of the evolved top right disc, obtained by fitting sigmoid functions to the radial intensity profiles where the direction angle is measured from 0° (right) in positive orientation.

As expected, reasonable rotational invariance is observed with the brute-force maximisation for all three values of α, preserving the round shapes during evolution, Fig. 2 (b, c, d). The evaluation of radii, Fig. 2 (e), confirms the excellent rotational symmetry of the Rouy-Tourin scheme for standard dilation, with an evolved disc radius of 23 in agreement with the theory, given that its radius in the initial image is 28, and 50 iterations with $\tau = 0.1$ amount to a structuring element radius of 5. The radius is shrunk faster with $\alpha < 1$ and slower with $\alpha > 1$. Fig. 2 (e) reveals slightly faster shrinkage in diagonal than in axial directions, as visible in the range $0^\circ \ldots 180^\circ$ (top two quadrants) where the disc evolves unperturbed by neighbouring structures, which indicates some further space for improvement in our discretisation of fractional derivatives.

The numerical dissipation due to the finite difference discretisation as evident in the standard dilation result (b) is well-known. As anticipated in Section 2.2, $\alpha > 1$ (c) mitigates it whereas $\alpha < 1$ (d) increases the blur. The non-locality of our fractional derivatives implies that they look into the depth of bright structures during fractional dilation. In our example, it is evident that standard dilation (b) evolves the discs roughly independently whereas fractional dilation (c, d) reacts to the initial proximity of the discs by speeding up for $\alpha > 1$ (c) or slowing down for $\alpha < 1$ (d) the inward movement of contours in the regions of proximity, leading to a slight repulsion between the discs in (c) and a slight attraction in (d). In Fig. 2 (e) the dents or peaks near directional angles of 218° (bottom left part of the top right disc) and 270° (bottom) reflect this effect.

Regarding the naive dilation results, Fig. 2 (f, g), we notice that the radial deviations from rotational symmetry (angular range $0^\circ \ldots 180^\circ$) are smaller for the naive method than for our proposed method in the case $\alpha > 1$ but more pronounced than with our approach in the case $\alpha < 1$. However, the non-locality effects with the naive method are highly direction-dependent: The repulsion in (f) is more pronounced in axial direction but almost absent in the diagonal direction, as confirmed by the different depth of the dents in Fig. 2 (e); notice that there is even a slight attraction effect in directions neighbouring to the diagonal 218° direction. The attraction in (g) is highly exaggerated in the axial direction but again much weaker in the diagonal direction; here, one sees also that by the interaction of the 1-D fractional derivatives in x and y direction

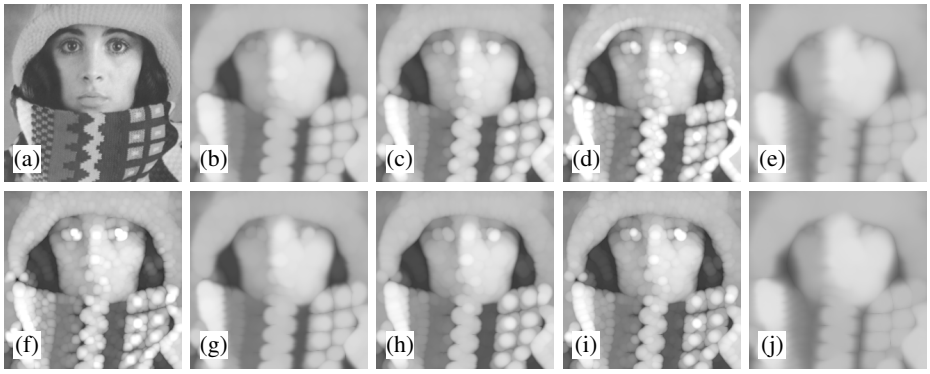

Fig. 4. Standard and fractional PDE-based dilation PDE of a grey-scale image. All dilations computed by an Euler forward scheme with time step size $\tau = 0.1$ and 100 iterations. **Top left to bottom right in rows:** (a) grey-scale image *trui*, 256×256 pixels; (b) standard dilation ($\alpha = 1$), brute-force maximisation; (c) fractional dilation, $\alpha = 1.25$, brute-force maximisation; (d) same but $\alpha = 1.5$; (e) same but $\alpha = 0.75$; (f) fractional dilation, $\alpha = 1.5$, naive composition of x and y derivatives; (g) standard dilation ($\alpha = 1$), gradient-guided computation; (h) fractional dilation, $\alpha = 1.25$, gradient-guided computation; (i) same but $\alpha = 1.5$; (j) same but $\alpha = 0.75$.

over the iteration steps an unnatural filling in happens in the roughly triangular region between the three discs. Comparing the evidence regarding rotational invariance of our proposed 2-D fractional dilation versus the naive 1-D based fractional dilation, it can be concluded that despite of an apparent slight advantage of the naive method in the case of an isolated contour (top quadrants) and $\alpha > 1$ the 2-D fractional dilation performs clearly better in the overall isotropic treatment of image structures.

The second image, Fig. 3(a), is designed to show the evolution of straight contours (on the left of each of the two white foreground objects) with structures of variable thickness behind, where the "depth-probing" effect of fractional derivatives is expected to appear. We see that standard dilation (b) propagates the straight left object contours at uniform speed. For $\alpha > 1$ (c) the propagation is accelerated where only thin bright layers back up the contour, leading to a progressively bumpy appearance of the propagated contour from top to bottom. For $\alpha < 1$ (d) an opposite effect is observed.

Real-world test image. For the following experiments we use a grey-scale image shown in Fig. 4(a). In our first experiment, Fig. 4, we compare different variants of fractional dilation for derivative orders greater and smaller than one with standard dilation. In particular, we compute dilation using brute-force maximisation of directional fractional derivatives and using the directional fractional derivative in the direction given by the standard gradient ("gradient-guided computation"). As expected, the results of both methods coincide for $\alpha = 1$; for other values of α the results are similar such that the gradient-guided method can be considered as an approximation of full maximisation. However, the effects of the fractional derivatives are more pronounced with the full maximisation since it finds the maximum of the fractional derivative with more accuracy. Comparing fractional to standard dilation, we observe the qualitative phenomena suggested by our consideration of the 1D case in Sec. 2.2: for fractional orders greater

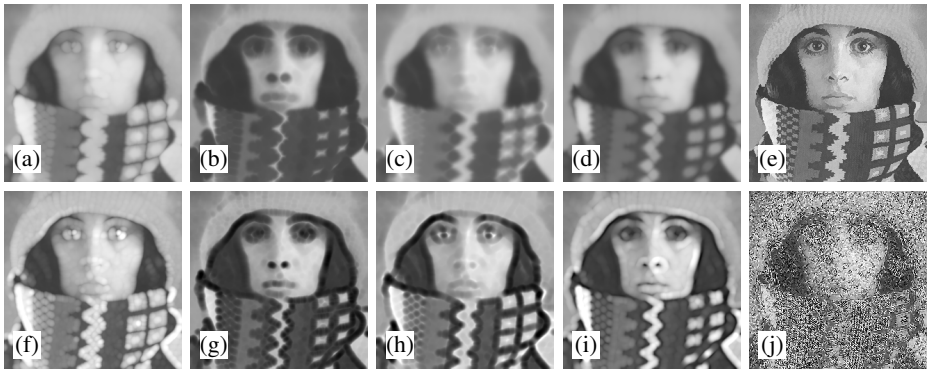

Fig. 5. Standard and fractional morphological filters for the grey-scale image *trui* from Fig. 4(a). All dilations/erosions computed by an Euler forward scheme with time step size $\tau = 0.1$, 50 iterations, and brute-force maximisation. **Top row:** (a–e) standard morphological filters ($\alpha = 1$). **Bottom row:** (f–j) fractional morphological filters, $\alpha = 1.5$. **Left to right:** (a, f) dilation; (b, g) erosion; (c, h) closing; (d, i) opening; (e, j) shock filter.

than one, an enhancement of edges and thin line structures and a reduction of numerical dissipation, and for a fractional order below one, contrast reduction and blurring. Note that all results reveal a reasonable degree of rotational invariance. To complement our comparison of methods, we give one result for the naive method which confirms its significant directional bias, evident from the blocky appearance of the dilated highlights.

Our next experiment, see Fig. 5, demonstrates the effects of simple and composed morphological operators: dilation, erosion, closing (by feeding the result of the dilation up to the desired evolution time into an erosion evolution that runs for the same time), opening (analogously) and a morphological shock filter. Given the strong dissipation with fractional order below one, we focus here on fractional orders above one as the more interesting case. Moreover, we choose a shorter evolution time than in the previous experiment. The shock filter of fractional order α with full maximisation is defined here as (fractional) dilation for locations where the directional derivative of order $\alpha + 1$ is negative, erosion where it is positive. Note that with our upwind-like discretisation of directional fractional derivatives of order $\neq 1$ the switch can be made simply dependent on the sign of $[|\boldsymbol{\nabla}^\alpha u|]_+ + [|\boldsymbol{\nabla}^\alpha u|]_-$, i.e. just computing the r.h.s. for the dilation and erosion evolution at each point and using the absolutely lesser of the two.

The effects of fractional erosion, closing and opening with order $\alpha = 1.5$ compared to their standard morphological counterparts are along the lines to be expected from our observations on dilation: more pronounced enhancement of contours, and lesser dissipation. In the closing it is interesting to note that due to the contrast enhancement of some minima (dark spots) in the dilation step, the subsequent erosion creates larger dark patches that are darker than in the original image; similarly for opening.

For the shock filter a fractional order $\alpha = 1.5$ is unfavourable in that it leads to the creation of many new extrema that are then enhanced in the process. We compare shock filter results for a broader range of derivative orders in Fig. 6. For $\alpha = 1.25$ the creation of additional extrema is already less pronounced than for $\alpha = 1.5$. In contrast,

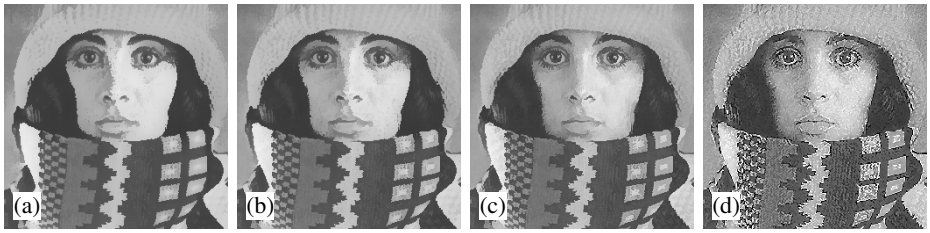

Fig. 6. Standard and fractional morphological shock filtering of the grey-scale image *trui* from Fig. 4(a). All evolutions computed by an Euler forward scheme, $\tau = 0.1$, 50 iterations, and brute-force maximisation. **Left to right:** (a) $\alpha = 0.5$; (b) $\alpha = 0.75$; (c) $\alpha = 1$; (d) $\alpha = 1.25$.

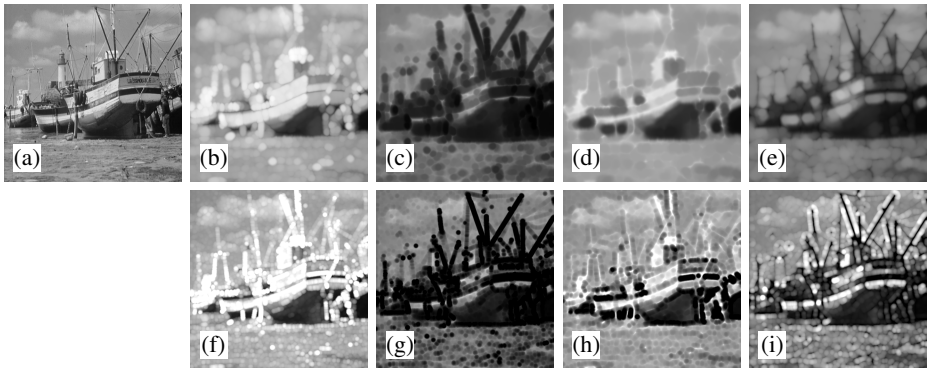

Fig. 7. Standard and fractional morphological filters. All dilations/erosions computed by an Euler forward scheme with time step size $\tau = 0.1$, 100 iterations, and brute-force maximisation. **Top row:** (a) grey-scale image *boats*, 512×512 pixels, (b–e) standard morphological filters ($\alpha = 1$). **Bottom row:** (f–i) fractional morphological filters, $\alpha = 1.5$. **Left to right:** (b, f) dilation; (c, g) erosion; (d, h) closing; (e, i) opening.

fractional orders below one turn out beneficial here as can be seen from the results for $\alpha = 0.75$ and $\alpha = 0.5$ where the segmentation-like effect of the standard ($\alpha = 1$) filter is even more pronounced, and both segments and their boundaries are visibly smoothed, apparently by the interaction of the blurring tendency of the fractional dilation and erosion for $0 < \alpha < 1$ with the shock-creating effect of the switch.

Finally, we show in Fig. 7 additional numerical results for a well-known test image *boats* comparing standard morphological filters ($\alpha = 1$) such as dilation, erosion, closing, and opening with fractional morphological filters using $\alpha = 1.5$.

4 Conclusion

We have established a framework for space-fractional PDE-based grey-scale morphology by replacing the spatial derivatives in the Hamilton-Jacobi PDEs describing morphological dilation and erosion with a fractional derivative. We have proposed a novel

variant of spatial fractional derivatives with spatial discretisations consequently designed to incorporate geometric invariance with respect to reflections and rotations. The discretisation is derived from developing fractional powers of a polynomial associated with an upwind-type first derivative stencil into a power series. As with all fractional derivative concepts, the infinite support requires a truncation. Approximation of fractional dilation and erosion PDEs then involves a one-dimensional optimisation problem for the advection direction. With this at our hand, higher morphological operations such as opening, closing, and shock filter are at our disposal. Numerical results confirm analytically predicted properties of the filters and show that the new method achieves better rotational invariance than conventional approaches.

Future work will be directed on one hand at improvements of the method, in particular more efficient ways to perform the optimisation over advection directions in (10) in order to avoid the brute-force optimisation used in most of our experiments so far, and on the other hand at a more extensive evaluation of the possible benefits of the space-fractional morphological filters for application problems. Moreover the choice of the truncation length for the fractional derivative stencils (which was fixed to 30 in our 2D image experiments) deserves additional investigation analytically and experimentally. Extensions of the approach to colour images and to non-Euclidean norms simulating non-disc-shaped structuring elements are other possible goals. Last but not least, the approach should be embedded into a broader view encompassing space-fractional derivatives for various image processing problems.

References

1. Arora, S., Mathur, T., Agarwal, S., Tiwari, K., Gupta, P.: Applications of fractional calculus in computer vision: A survey. Neurocomputing **489**, 407–428 (2022)
2. Beyer, H., Kempfle, S.: Definition of physically consistent damping laws with fractional derivatives. Zentralblatt für angewandte Mathematik und Mechanik **75**(8), 623–635 (1995)
3. van den Boomgaard, R., Smeulders, A.: The morphological structure of images: the differential equations of morphological scale space. IEEE Transactions on Pattern Analysis and Machine Intelligence **16**(11), 1101–1113 (1994)
4. Brockett, R.W., Maragos, P.: Evolution equations for continuous-scale morphology. IEEE Transactions on Signal Processing **42**(12), 3377–3386 (1994)
5. Chen, S., Liu, F., Turner, I., Anh, V.: A fast numerical method for two-dimensional Riesz space fractional diffusion equations on a convex bounded region. Applied Numerical Mathematics **134**, 66–80 (2018)
6. Chowdhury, M.R., Qin, J., Lou, Y.: Non-blind and blind deconvolution under Poisson noise using fractional-order total variation. Journal of Mathematical Imaging and Vision **62**, 1238–1255 (2020)
7. Didas, S., Burgeth, B., Imiya, A., Weickert, J.: Regularity and scale-space properties of fractional high order linear filtering. In: Kimmel, R., Sochen, N., Weickert, J. (eds.) Scale Space and PDE Methods in Computer Vision, Lecture Notes in Computer Science, vol. 3459, pp. 13–25. Springer, Berlin (2005)
8. Failla, G., Zingales, M.: Advanced materials modelling via fractional calculus: challenges and perspectives. Philosophical Transactions of the Royal Society A **378**, 20200050 (2020)
9. Guichard, F., Maragos, P., Morel, J.M.: Partial differential equations for morphological operators. In: Bilodeau, M., Meyer, F., Schmitt, M. (eds.) Space, Structure and Randomness:

Contributions in Honor of George Matheron in the Field of Geostatistics, Random Sets and Mathematical Morphology, pp. 369–390. Springer, New York (2005)
10. Hao, Z., Sun, Z., Cao, W.: A fourth-order approximation of fractional derivatives with its applications. Journal of Computational Physics **281**, 787–805 (2015)
11. He, N., Wang, J.B., Zhang, L.L., Lu, K.: An improved fractional-order differentiation model for image denoising. Signal Processing **112**, 180–188 (2015)
12. Huang, G., Qin, H., Chen, Q., Shi, Z., Jiang, S., Huang, C.: Research on application of fractional calculus operator in image underlying processing. Fractal and Fractional **8**, 37 (2024)
13. Kleefeld, A., Vorderwülbecke, S., Burgeth, B.: Anomalous diffusion, dilation, and erosion in image processing. International Journal of Computer Mathematics **95**, 1375–1393 (2018)
14. Meerschaert, M.M., Tadjeran, C.: Finite difference approximations for two-sided space-fractional partial differential equations. Applied Numerical Mathematics **56**, 80–90 (2006)
15. Oldham, K.B., Spanier, J.: The Fractional Calculus. Dover, New York, 2nd edn. (2006)
16. Ortigueira, M.D.: Riesz potential operators and inverses via fractional centred derivatives. International Journal of Mathematics and Mathematical Sciences **2006**, 48391 (2006)
17. Pan, K., Sun, H.W., Xu, Y., Xu, Y.: An efficient multigrid solver for two-dimensional spatial fractional diffusion equations with variable coefficients. Applied Mathematics and Computation **402**, 126091 (2021)
18. Podlubny, I.: Fractional Differential Equations. Academic Press, San Diego (1999)
19. Podlubny, I., Chechkin, A., Skovranek, T., Chen, Y.Q., Vinagre Jara, B.M.: Matrix approach to discrete fractional calculus II: partial fractional differential equations. Journal of Computational Physics **228**, 3137–3153 (2009)
20. Schäfer, I., Kempfle, S.: Impulse responses of fractional damped systems. Nonlinear Dynamica **38**, 61–68 (2004)
21. Shukla, A.K., Pandey, R.K., Pachori, R.B.: A fractional filter based efficient algorithm for retinal blood vessel segmentation. Biomedical Signal Processing and Control **59**, 101883 (2020)
22. Sparavigna, A.C.: Fractional differentiation based image processing. Tech. Rep. cs.CV:0910.2381v4, arXiv.org (2015)
23. Tuan, N.H., Aghdam, Y.E., Jafari, H., Mesgarani, H.: A novel numerical manner for two-dimensional space fractional diffusion equation arising in transport phenomena. Numerical Methods for Partial Differential Equations **37**, 1397–1406 (2021)
24. Wu, T., Wan, S., Feng, C., Zhang, H., Zeng, T.: Blind image deconvolution: When patch-wise minimal pixels prior meets fractional-order method. Journal of Mathematical Imaging and Vision **67**, 3 (2025)
25. Xu, X., Dai, F., Long, J., Guo, W.: Fractional differentiation-based image feature extraction. International Journal of Signal Processing, Image Processing and Pattern Recognition **7**(6), 51–64 (2014)
26. Yang, Q., Chen, D., Zhao, T., Chen, Y.: Fractional calculus in image processing: a review. Fractional Calculus and Applied Analysis **19**(5), 1222–1249 (2016)
27. Yu, Y., Gao, Q., Zhao, X., Ji, Y.: 2-D modeling and analysis of time-domain electromagnetic anomalous diffusion with space-fractional derivative. IEEE Transactions on Geoscience and Remote Sensing **61**, 2000213 (2023)
28. Zhang, H., Liu, F., Anh, V.: Galerkin finite element approximation of symmetric space-fractional partial differential equations. Applied Mathematics and Computation **217**, 2534–2545 (2010)
29. Zhang, X., Li, R., Hong, J., Zhou, X., Xin, N., Li, Q.: Image-enhanced single-pixel imaging using fractional calculus. Optics Express **30**(1), 81–91 (2022)